Advanced Functional Materials / Volume 33, Issue 46 / 2305275

Research Article | Full Access

Liquid Nitrogen Temperature Mechanoluminescence and Persistent Luminescence

Xueqing Liu, Liangliang Zhang, Dandan Wang, Dengkui Wang, He Shen, Hao Wu, Huajun Wu, Guohui Pan, Zhendong Hao, Feng Liu, Jiahua Zhang

First published: 03 August 2023
https://doi-org.fgul.idm.oclc.org/10.1002/adfm.202305275
Citations: 1

Abstract

As novel stress-sensing materials, the reported mechanoluminescence (ML) phosphors work only at or above room temperature. Herein, the ML response to low temperatures (77 K) is extended by employing ultra-shallow traps. Strong ML stimulated by handwriting force followed by persistent luminescence is observed in $BaSi_2O_2N_2:Eu^{2+}$ (BSON) at 77 K. The UV pre-irradiated BSON can still keep the characteristics of ML with 45% intensity after 300 min. Abundant ultra-shallow traps with depth of ≈0.19 eV are found and revealed to be responsible for the low-temperature ML and persistent luminescence. Manipulation of the ultra-shallow traps is realized by doping Ge, Er, and Ce ions in BSON, leading to significant ML enhancement at 77 K. Together with ML, the ultra-shallow traps also exhibit force memory ability to replicate the pre-applied force pattern simply by afterglow. The finding advances the state-of-the-art in force sensing under low temperature conditions.

1 Introduction

Cryogenics has raised various new physical properties that only occur at low temperatures to inspire many amazing applications, such as cryotherapy, superconductor, and shrink-welding. In these applications, elastic biological tissues or mental structural materials become brittle at low temperatures and experience additional freezing force. Therefore, real-time monitoring the structural health[1] or stress distribution[2] is an urgent need for cryogenic applications. Mechanoluminescence (ML) phosphor[3-6] is a promising candidate

as a novel "smart" stress sensing/imaging material.[7-10] For example, in a typical biomechanical analysis, ML phosphor was pasted on a tooth surface[11] and could map submicron-sized microcracks under only 25 N masticatory force. For engineering structure diagnosis, a typical case was attaching the ML phosphor to the outer surface of ahigh-pressure vessel[12] to detect the position and depth of a 24 mm inner crack under 45 Mpa liquid pressure. Up to now, most ML phosphors are designed for stress sensing/imaging at room temperature or above.[13-25] Therefore, exploring ML phosphors that respond at low temperatures is urgently needed by cryogenic applications.

ML is involved in electrons released from traps by mechanical stimulation.[26] The trap depth, which can be determined by thermoluminescence (TL) peak, classifies the traps as shallow, medium or deep.[27, 28] Therefore, ML at or above room temperature involves traps with depths larger than 300 K. However, at low temperatures, the minimum trap depth involved decreases ≈4 times to 77 K in liquid nitrogen (LN_2) and ≈71 times to 4.2 K in liquid helium. These ultra-shallow traps associated with low temperatures, on the one hand, can release trapped charges in response to tiny stress and, on the other hand, are thermally excited to show the afterglow of ML.[29] The afterglow originating from ultra-shallow traps is important for application because it can visualize the force-changing moment by a long-lasting luminescence.[30, 31] Up to now, these ultra-shallow traps are poorly understood because most ML phosphor, for example the most studied $SrAl_2O_4:Eu^{2+}$ (SAO), do not have ultra-shallow traps. Therefore, to find an ML phosphor with ultra-shallow traps is a challenge.

$BaSi_2O_2N_2:Eu^{2+}$(BSON) is an oxynitride cyan emitting phosphor that naturally owns many defect species,[32] such as O vacancies, N vacancies, and N substituting O, to generate continuously distributed traps for ML.[33] The known traps in BSON distribute in a temperature range of 300 K–500 K and are divided into two parts: a shallow group center at 330 K and a deep group center at 368 K.[34] The deep traps in BSON are found essential to provide many new ML mechanisms. For example, Zhuang[35, 36] reported a new force-induced charge carrier storage effect of the deep traps to realize instantaneous photon emission in BSON. Petit[37] reported the reshuffling of deep trap occupations in BSON to memorize a mechanical event for more than 72 h. BSON was also found to have ML response to various mechanical stimulation,[38] such as friction, pressure, and tearing. Kersemans[39] even found BSON has ML response to the ultrasound, and they measured the 3D spatial radiation field of an ultrasonic transducer by BSON. Michels[40] further showed that the response frequency range of BSON to ultrasound is 1 MHz-25 MHz with a high spatial resolution of 170 µm. Overall, the continuously distributed traps in BSON make it a perfect ML phosphor. However, current studies performed at room temperature cannot offer information of ultra-shallow traps.

In this paper, we find ultra-shallow traps in BSON. The ML and persistent luminescence properties in BSON are studied at 77 k compared to that in SAO with only room temperature traps. Besides low-temperature response, ultra-shallow traps show other excellent features,

such as the force memory effect and IR response. Furthermore, we realize the manipulation of the ultra-shallow traps in BSON by doping various rare earth ions.

2 Results and Discussion

2.1 Crystal Structure and Defects

The synthesized sample shows a typical BSON phase, as the XRD pattern in **Figure** 1a shows. However, two diffraction peaks at 12.34° and 24.78° have a much higher intensity than the pattern from ICSD 419450. The Miller indices of the two peaks are (200) and (400), suggesting preferred orientation along [100] direction. In the Rietveld refinement process, the calculated intensity of the two peaks is still much weaker than the measured one, leading to a large χ^2 of 20.4. After correcting for preferred orientation along [100], the intensity of the two peaks increases, and χ^2 decreases to 6.07. The SEM image in Figure 1b proves the BSON particle has a needle-like shape. The HRTEM shows the preferred lattice plane has a d-spacing of ≈7.2 Å, exactly (200). The detailed measurements are shown in Figure S1 and S2 (Supporting Information). In addition, the elements Ba, Si, O, and N are homogeneously distributed inside the particle, indicating good synthesis of the phosphor. Overall, the synthesized BSON sample has needle-like particles that prefer to grow along the [100] direction.

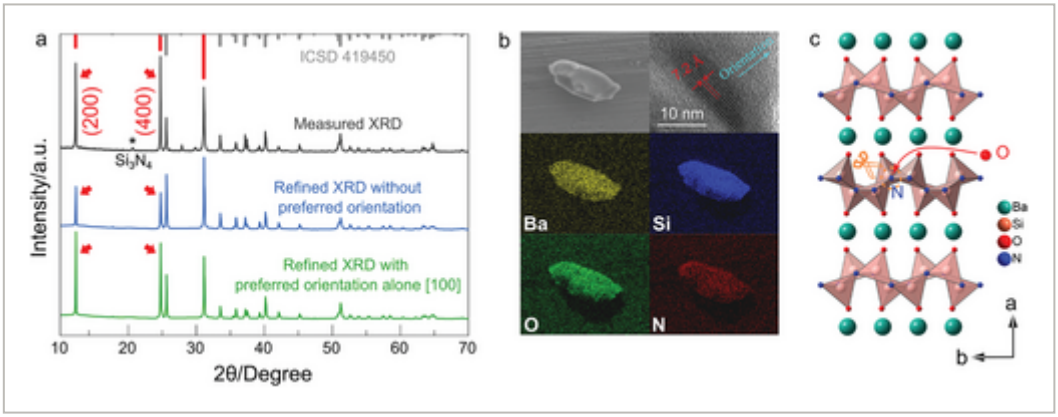

Figure 1

Open in figure viewer | PowerPoint

Crystal structure. a) The measured and refined XRD of BSON. b) SEM, HRTEM, and elemental mapping measurement of BSON; c) Crystal structure of BSON looking alone c axis.

The crystal structure of BSON shows a sandwich-like arrangement alone [100] (a axis), as shown in Figure 1c. Three [SiN_3O] tetrahedrons connect by one bridging N atom to form layers, which are joined by Ba atom alone [100]. The first principles calculation shows the defect formation energy of O substituting N () is only −0.89 eV, indicating easy to substitute N by O. Upon substitution of an N atom, three [SiN_2O_2] tetrahedrons are formed and

connect to one another by a bridging O atom, which is suggested to be metastable according to Pawling's second rule (electrostatic valency principle). The [SiN_3O] tetrahedron layers are inferred to be easily broken down due to the defect, while the Ba connection alone [100] is still intact. Therefore, the crystal tends to grow alone [100] direction. Furthermore, the defect formation energy of some defects in BSON, such as O vacancy, N vacancy, N substituting O, and N-O antisite defect, are calculated in the range of 2.5 eV–6.15 eV, as shown in Table S1 and Figure S3 (Supporting Information). The small formation energy for these defects provide a structure basis for continuously distributed ultra-shallow traps.

2.2 Persistent Luminescence and Mechanoluminescence at 77 K

BSON is a green phosphor and exhibits intense green afterglow at room temperature (RT).[32, 33, 41, 42] The photoluminescence (PL) and afterglow originate from Eu^{2+} emission, as shown in Figure S4 (Supporting Information). **Figure** 2a illustrates that the BSON afterglow persists for more than 480 s after the excitation stops. However, compared to the well-known long afterglow phosphor SAO, BSON decays much faster. Figure 2b displays the afterglow decay curves of BSON and SAO. The initial intensity of BSON is only ≈60% of SAO, and it drops to the background level more quickly. We attribute this phenomenon to the smaller number of RT traps in BSON than SAO. As shown in Figure 2c, BSON has a much weaker TL intensity at 300–400 K compared with SAO. Surprisingly, the liquid nitrogen temperature (77 K) afterglow of BSON is stronger and lasts longer than SAO. BSON afterglow is still visible at 120 s after the excitation stops, while SAO afterglow disappears, as shown in Figure 2d. The afterglow decay curve of BSON shows an initial intensity of 1.4 times that of SAO and a slower decay rate, as shown in Figure 2e. We observe a significant increase in TL intensity at 80–300 K for BSON, which is 13.9 times higher than at RT, as shown in Figure 2f. Therefore, we infer a larger quantity of ultra-shallow traps inside BSON than the RT traps. For comparison, SAO only shows a slight increase in TL intensity at 250–300 K, indicating few ultra-shallow traps in SAO. Therefore, we infer the ultra-shallow traps in the depth of 80–200 K are responsible for the different afterglow performance between BSON and SAO at 77 K.

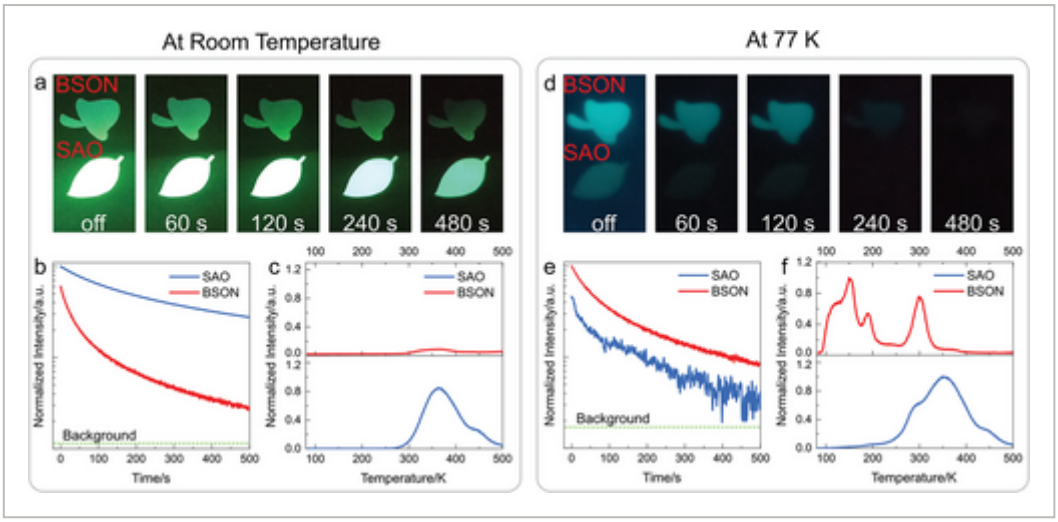

Figure 2

Open in figure viewer | PowerPoint

Afterglow of BSON and SAO. a,d) Afterglow photograph of BSON and SAO at RT a) and 77 K d). b,e) Afterglow decay curves of BSON and SAO at RT b) and 77K e). c,f) TL curves of BSON and SAO at RT c) and 77 K f). All the samples are pre-irradiated by 254 nm UV lamp for 4 min at RT or 77K.

We use the initial rise method to determine the trap depth in this case, as shown in **Figure** 3. Figure 3a shows that the shoulder peak at ≈125 K vanishes when the preheating temperature rises from 103 K to 123 K. Likewise, the glow peak at ≈150 K vanishes when the preheating temperature rises from 123 K to 143 K. As we increase the preheating temperature by 20 K each time, some glow peaks disappear from the TL curve. This phenomenon indicates the traps to be continuously distributed in depth, because a 20 K temperature interval corresponds to only 1.9 meV in energy. This phenomenon is also consistent with SAO in Figure 3d, which has a continuous trap depth distribution.[43, 44] The initial rise method can provide a more reliable estimate of trap depth for such traps.[45, 46] **Figure** 3b, 4e are the Arrhenius plots (Ln[I] versus 1/T) of the TL glow for initial rise analysis, where the slope of the initial rising part is the trap depth. As shown in Figure 3c, the calculated trap depth of BSON varies from 0.19 eV to 0.55 eV. Compared with the trap depth of SAO in Figure 3f, BSON has many traps with depths smaller than 0.48 eV. Therefore, we define ultra-shallow traps as those with depths smaller than 0.48 eV in this case.

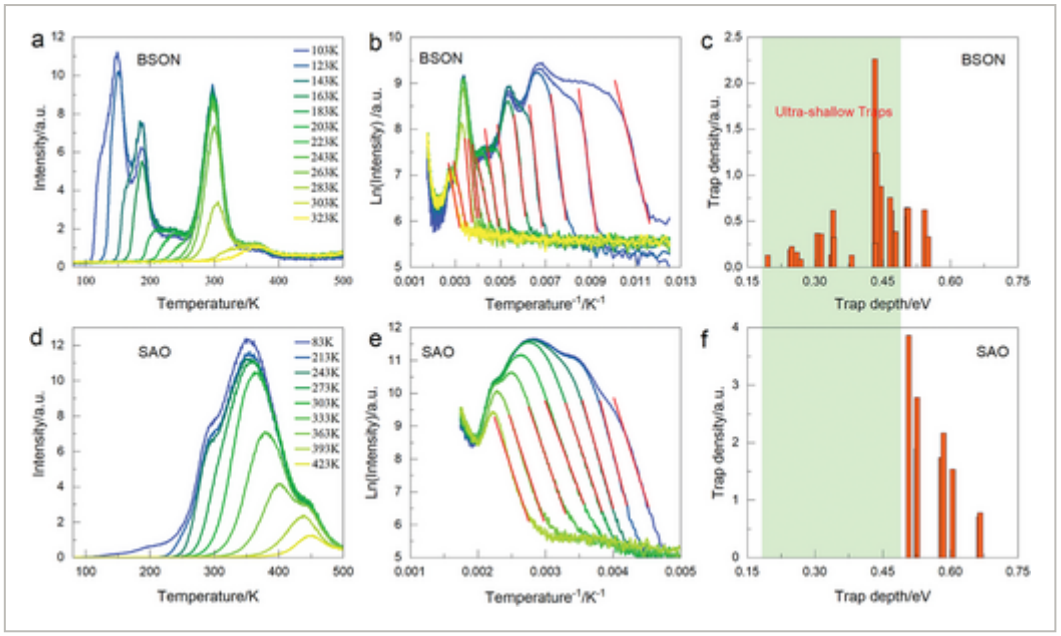

Figure 3

Open in figure viewer | PowerPoint

Determining the trap depth inside BSON (Top) and SAO (Below). a,d) TL curves of BSON and SAO that preheated at different temperature. b,e) Arrhenius plot of the TL curves for initial rise analysis. c,f) The estimated trap depth by initial rise method.

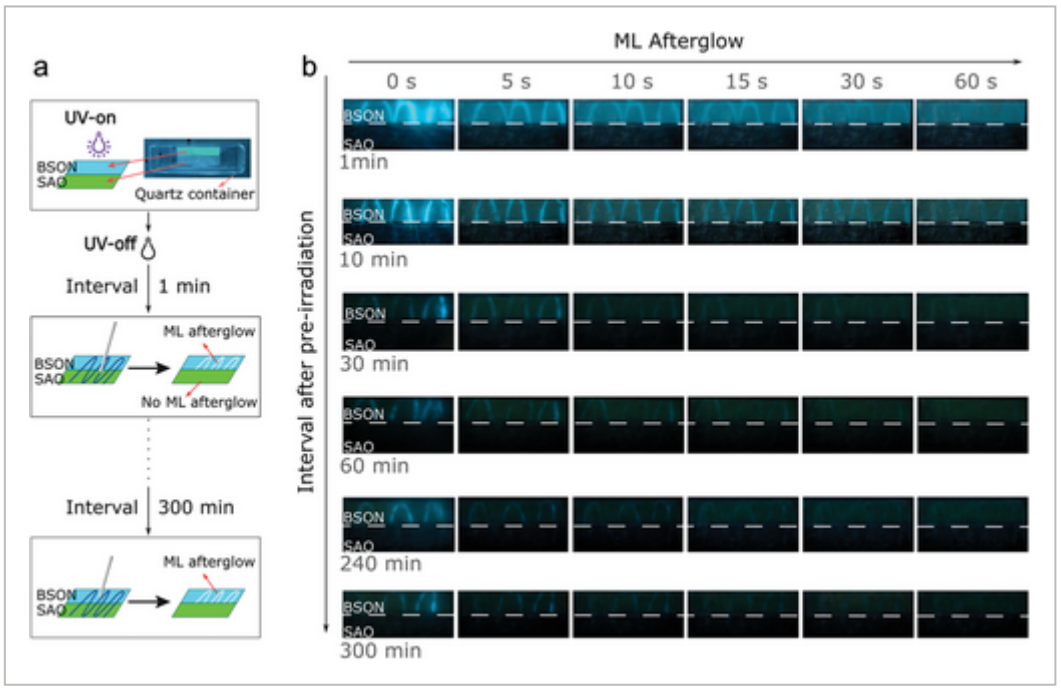

Figure 4

Open in figure viewer | PowerPoint

ML of BSON and SAO at 77 K. a) Diagram of the experimental setup. b) Photograph of the ML afterglow. The rows of the photograph matrix show ML afterglow and the columns show ML response at different intervals. All the samples are

pre-irradiated by 254 nm UV lamp for 15 min at 77K.

To investigate ML property at 77 K, BSON phosphor film and SAO phosphor film with size of 1 × 4 cm are placed side by side and are pre-irradiated under a 254 nm UV lamp for 15 min in LN_2, as shown in Figure 4a. Then, we turn off the UV lamp and use a glass rod to draw curves on the film surface by hand at different intervals. Only BSON film responds to the weak force of handwriting, while SAO does not. In the first column of Figure 4b, we can find the ML intensity at different intervals decreases very slowly and maintains ≈45% at an interval of 300 min. Figure S8 (Supporting Information) shows the detailed slow decrease of ML intensity to prove that ultra-shallow traps can store electrons for a long time at 77 K. The first row of Figure 4b shows the ML afterglow, the persistent luminescence originates from electrons released by mechanical stimulation, to be observed by the naked eye within 60 s, and the afterglow of BSON also creates a bright background that obscures the ML signal. At an interval time of 10 min, the light background decayed to show a clearer ML signal. The ML afterglow is important to record the moving trail for a long time without complex monitoring equipment. Figure S7 (Supporting Information) summarizes the detailed change in ML afterglow intensity at each intervals. Besides the ML response at 77 K, we infer similar ML response maintains even at a temperature as low as 4.2 K (liquid helium temperature). Because we detect a large amount of even shallower traps in 10 K–77 K temperature range, as shown in Figure S9 (Supporting Information). Unfortunately, we could not conduct ML experiments at such low temperatures due to experimental limitations at this stage. Overall, BSON has many ultra-shallow traps that make it promising for cryogenic applications.

2.3 Property of Ultra-shallow Traps

Manipulation of these ultra-shallow traps is possible by doping various ions. As shown in Figure S10 (Supporting Information), 15 kinds of ions are exploded to show changes in the number of traps by TL curve. Representative, Ge-doping increases the number of ultra-shallow traps at a depth of 80 K–130 K (Peak I), resulting in a ≈3 times increase in TL intensity, as shown in **Figure** 5a. The inserted photograph shows that the ML intensity from Ge-doped BSON is significantly stronger. Similarly, Er-doping increases the number of ultra-shallow traps at a depth of 130 K-200 K (Peak II and Peak III), resulting in a ≈2 times increase in TL intensity, as shown in Figure 5b. The ML intensity from Er-doped BSON also becomes stronger. Ce increases the number of traps at a depth of 180 K–250 K (Peak III and Peak IV), resulting in a ≈1.5 times increase in TL intensity as shown in Figure 5c. The inserted photograph shows that the ML intensity from Ce-doped BSON is still stronger. Gd-doping increases the number of traps at a depth of 250 K–400 K (Peak V), resulting in a ≈1.4 times increase in TL intensity as shown in Figure 5d. However, the ML intensity of Gd-doped BSON is marginally lower than that of non-doped BSON due to a slight decrease in peak I. Figure S11 (Supporting Information) shows the detailed influence of Ge, Er, Ce, and Gd on ML performance. First principles calculation shows that ion co-doping influences the defect formation energy. For example, Ge co-doping significantly reduces formation energy from

6.01 eV to 3.89 eV and slightly reduces other trap formation energy; Similarly, Ce co-doping only dramatically reduces formation energy from 6.15 eV to 3.29 eV. However, it is still difficult to tell precisely the origin of every trap at the current stage for its complexity. The detailed trap formation energy after Ge, Er, Ce, and Gd co-doping is shown in Table S2 and Figure S12–S15 (Supporting Information). Overall, the ultra-shallow traps identified as Peak I, II, and III in TL curve (<200 K) have different origins, but all contribute to ML response at 77 K, and the RT traps identified as Peak V in TL curve do not.

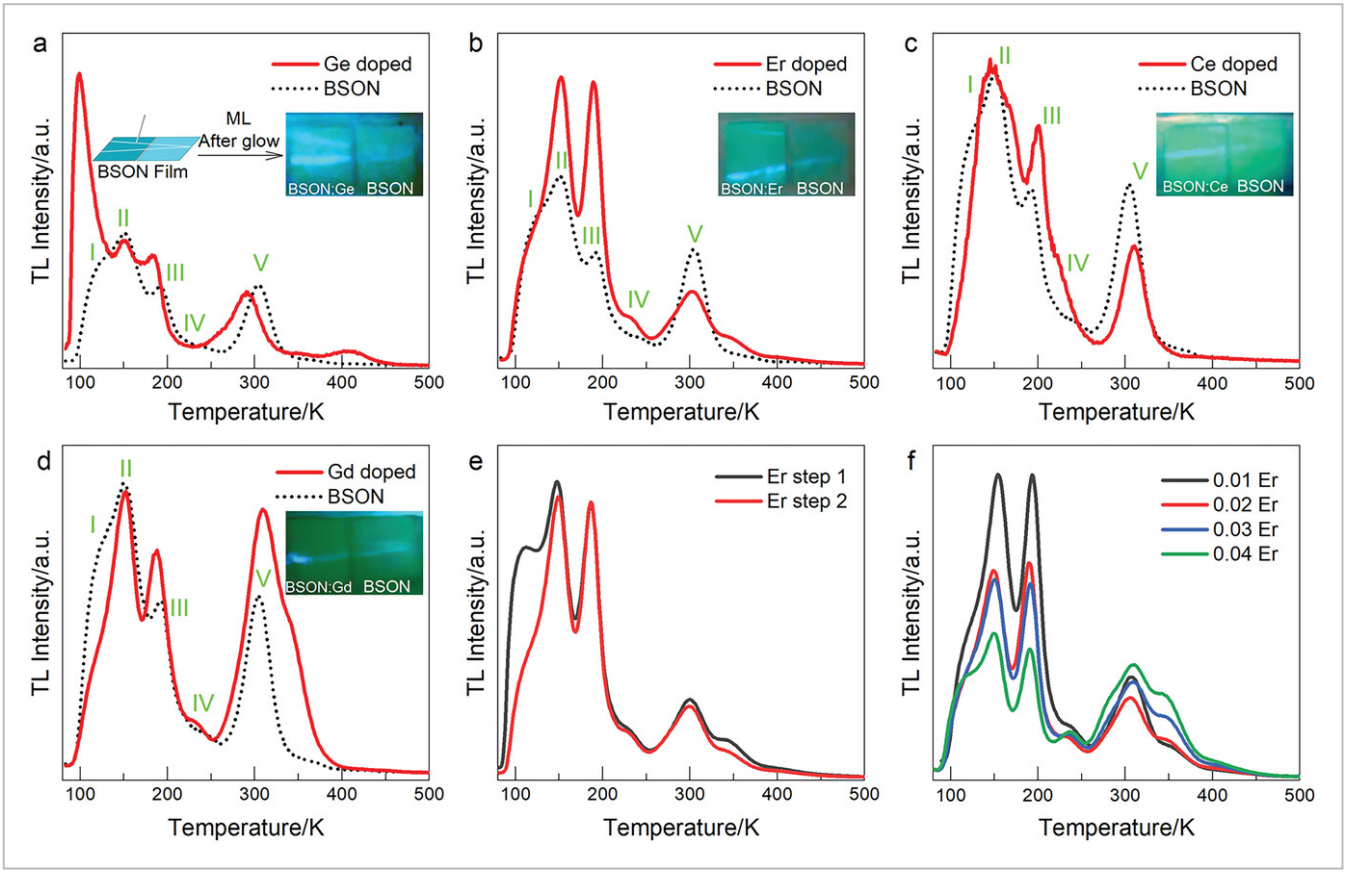

Figure 5

Open in figure viewer | PowerPoint

TL curve of BSON doped with Ge a), Er b), Ce c), and Gd d). The photograph shows ML afterglow of different ion doped BSON film (2 × 2 cm) taken 15 min after pre-irradiation. e) TL curve of BSON with Er introduced at different synthesis step. f) TL curve of BSON with different Er concentration.

Figure 5e demonstrates that the number of ultra-shallow traps is susceptible to the synthesis method. In the two-step synthesis of BSON, in this case, doping Er at the first step introduces much more ultra-shallow traps in the depth of 80 K–130 K (peak I) than doping Er at the second step. The number of ultra-shallow traps is also influenced by Er concentration. As shown in Figure 5f, the higher concentration of Er, the fewer ultra-shallow traps in the depth of 130 K–200 K (Peak II and Peak III). With Er concentration increase from 1% to 4%, the TL intensity decreases ≈2.5 times. However, the number of RT traps increases with Er. TL

intensity at 250 K–400 K (Peak V) increases ≈1.5 times with increasing Er concentration. Overall, ultra-shallow traps are more sensitive to doping ions and synthesis than RT traps.

Figure 6a shows the charging process of the ultra-shallow traps. As the charging time increases from 60 s to 300 s, the TL intensity of peak I and peak V increases by ≈5.2 times and ≈2.3 times, respectively. This increase suggests that ultra-shallow traps have a slower electron capture rate and therefore require more time to charge. The position of TL peak I remains almost unchanged, but peak II shifts from 146 K to 137 K, peak III shifts from 185 K to 176 K, and peak V shifts from 300 K to 293 K. This phenomenon indicates the existence of a multi-order kinetic process.[47] The traps are also found more effectively filled at 77 K than at RT, as shown in Figure S19 (Supporting Information). Figure 6b shows the ultra-shallow traps is IR responsible. TL peaks below 147 K are completely emptied in a short time under 980 nm IR irradiation. However, some ultra-shallow traps ≈200 K retain electrons even though much deeper traps at 300 k are almost empty. This phenomenon persists when we raise the measurement temperature to 147 K. Thus, some ultra-shallow traps ≈200 K have slower empty speed by IR irradiation than RT traps.

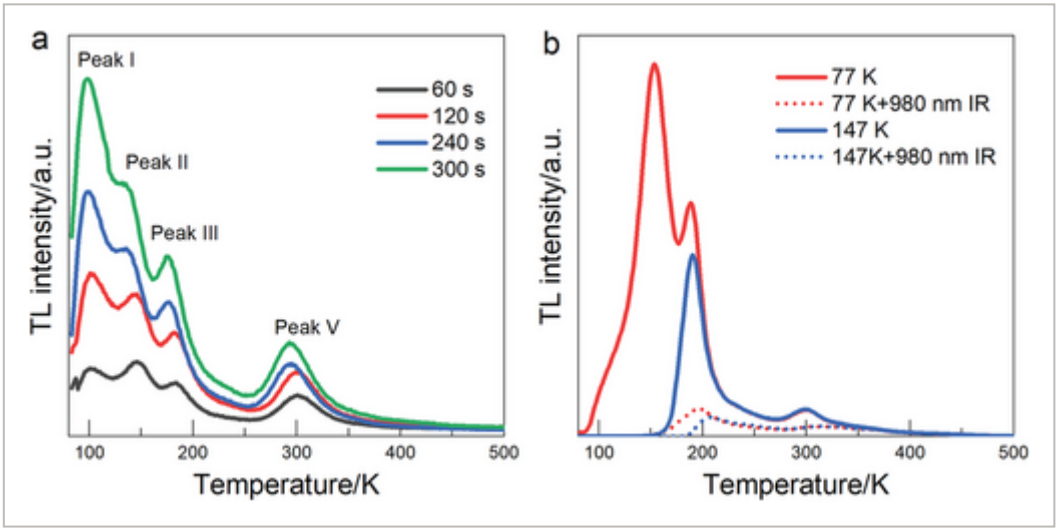

Figure 6

Open in figure viewer | PowerPoint

a) TL curve of BSON with different charging time. b) TL curve before and after IR stimulation (980 nm irradiation for 1 min) at 77 and 147 K.

Figure 7 shows the pressure memory effect of ultra-shallow traps that can be optically detected. We apply a mechanical force of 1.5 Mpa to a thermally emptied BSON film at room temperature and then charge it for 2 min under a 254 nm UV lamp at 77k, as shown in Figure 7a. When the UV lamp is turned off, the pattern of the pre-applied force becomes visible due to its higher afterglow intensity compared to zones without pre-applied force. The pattern is visible within 60 s. Figure 7b shows that the force zone has both a higher afterglow intensity and a slower decay rate. Therefore, the force zone is more obvious in a

15–50 s time interval. In the TL spectra, a new and intense peak at 250 K is observed to indicate forming of new ultra-shallow traps by applying pressure, as shown in Figure 7c. Since the force is applied before charging, it can be inferred that pressure alters the number of traps rather than the distribution of electrons within them. This phenomenon differs from that of Petit,[37] who applies pressure after charging to only change the electron distribution inside deep traps. In contrast to Petit's work, where the force is detectable under 980 nm radiation or at elevated temperatures, we can easily observe it through the afterglow without other stimulation. Figure S16 (Supporting Information) illustrates that we can still use 980 nm radiation to detect the pre-applied force after the afterglow fades away. In summary, pressure has a much greater effect on ultra-shallow traps than on deep traps. Together with the pressure memory effect, PL intensity of BSON decreases. Figure 7d illustrates this decrease, which agrees with the assumption that more traps are formed to capture excited electrons, resulting in reduced PL intensity.

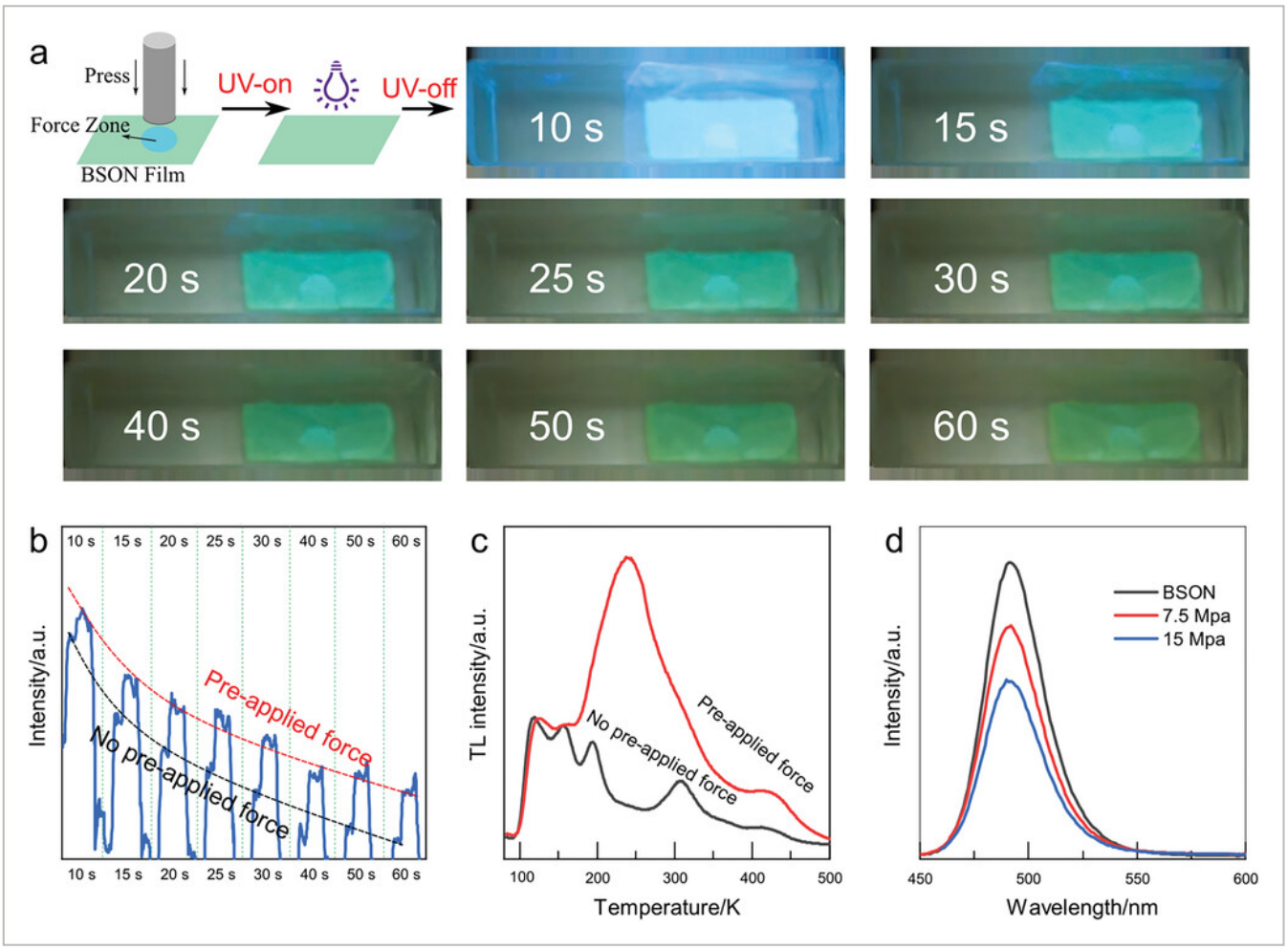

Figure 7

Open in figure viewer | PowerPoint

Pressure memory effect. a) Afterglow photograph of the BSON film (2 × 4 cm) to show the pre-applied force pattern (ϕ = 1 cm). b) Afterglow intensity of the BSON film at zones with pre-applied force (red) or not (black). c) TL curve of BSON with pre-applied force (red) or not (black). d) PL spectra of BSON under different prior mechanical force.

Exploring the ML response at low temperatures can meet cryogenic applications' structural health monitoring and stress distribution measurement. For example, BSON may be used to show the stress distribution of the metal components when performing cold shrink assembly in the automotive industry. Or, BSON may be used to monitor the structural health of Liquefied Natural Gas (LNG) or hydrogen storage facilities. In low-temperature space environments, the force memory ability may be used to detect minor impacts at the spacecraft surface.

3 Conclusion

In summary, we find ultra-shallow traps in the $BaSi_2O_2N_2:Eu^{2+}$ (BSON) phosphor to generate mechanoluminescence (ML) and followed by persistent luminescence at 77 K. Many defects in the BSON phosphor, including O vacancies, N vacancies, N replacing O, and N-O antisite defects, provide the structural basis for constantly distributed ultra-shallow traps. We detected bright ML at 77 K followed by an ML afterglow lasting more than 60 s. The ultra-shallow traps are identified as those with depths smaller than 200 K based on the TL curve or 0.19–0.48 eV estimated by the initial rise method. The ML intensity can retain ≈45% of the initial even 300 min after the pre-irradiation stops. Ion co-doping changes the quantity of ultra-shallow traps to realize trap manipulation. For example, Ge-doped BSON increases the number of ultra-shallow traps in depths of 80 K–130 K; Er increases the number of ultra-shallow traps in depths of 130 K–200 K; Ce increases the number of traps in depths of 180 K–250 K. Besides low-temperature response, ultra-shallow traps also show a strong memory to the pre-applied force and reproduce the force trace by afterglow. Furthermore, judging from the TL curves, we infer BSON can apply to even lower temperatures of liquid helium (4.2 K). Further investigations are desired for urgent needs from cryogenic applications.

4 Experimental Section

Preparation of $BaSi_2O_2N_2:0.02Eu^{2+}$ Phosphor

$BaSi_2O_2N_2:0.02Eu^{2+}$ phosphor was synthesized by a two-step method. In the first step, $Ba_2SiO_4:0.02Eu^{2+}$ was synthesized as a precursor. The stoichiometric ratio of $BaCO_3$ (99.99%), SiO_2 (99.99%), and Eu_2O_3 (99.99%) were weighed and ball ground for 24 h. Then, the mixture was dried and collected into an alundum crucible for calcination in a tube furnace. The sintering temperature was 1200 °C for 6 h in an air environment. When cooled to room temperature, the final product with green body color was ground and washed as raw materials. In the second step, the stoichiometric ratio of $Ba_2SiO_4:0.02Eu^{2+}$ and Si_3N_4 (99.99%) were weighed as raw materials and ground in an agate mortar for 20 min. The mixture was then sintered in a tube furnace at 1400 °C for 4 h with the protection of flowing 5% H_2/N_2 gas mixture. The heating rate was set at 3 °C min^{-1}. After cooling to room

temperature, the sample was ground and washed with deionized water to get the final $BaSi_2O_2N_2$:0.02Eu^{2+}phosphor.

Characterization

The powder diffraction data were collected by Bruker D8 Focus X-ray diffraction instrument with a Cu target source (40 kV, 40 mA). The photoluminescence spectra, afterglow decay curves, and thermoluminescence (TL) curves were measured by FLS900 spectrometer (Edinburgh Instruments, U.K.) combined with THMS600E cooling-heating platform (77–873 K, Linkam Scientific Instrument, U.K.). All the TL curves were measured with the heating rate fixed to 2 K s^{-1}. The photographs were captured by 8.3MP 1/1.2′′ Sony Exmor CMOS sensor. The SEM image and elemental mapping were measured by Hitachi, S-4800 emission scanning electron microscopy equipped with EDAX Genesis 2000 energy disperse spectroscopy. The HRTEM and electron diffraction pattern were measured by transmission electron microscopy (Talos F200S) with an accelerating voltage of 200 kV.

Calculation

The first principles calculations were performed by Vienna Ab-initio simulation package (VASP) program. The projector-augmented-wave (PAW) method was used, and the Perdew-Burke-Ernzerhof (PBE) exchange-correlation functional of the generalized gradient approximation (GGA) was utilized to describe the electron interactions. The cut-off energy set for the plane wave basis was 400 eV, and a 2 × 2 × 4 Monkhorst-Pack k-point in the Brillouin zone was sampled. Moreover, the convergence criterion for energy was set to 10^{-4} eV, and for force was 10^{-2} eV $Å^{-1}$. The defect formation energy (E^f) of different doping or vacancy defects was calculated based on the definition of E^f : $E^f = E_{defect} – E_{pri} – \sum n_i \mu_i$, where E_{defect} is the energy of the $BaSi_2N_2O_2$ with doping or vacancy defects, E_{pri} is the energy of the pristine $BaSi_2N_2O_2$, n_i is the number of element *i* and μ_i is the corresponding chemical potential of element *i*. Herein, μN, and μ_O are the energy of a single N and Si atom, respectively calculated from the total energy of isolate N_2 and O_2 molecule: $\mu N = \mu(N_2)/2$, $\mu_O = \mu(O_2)/2$.

Acknowledgements

This work was financially supported by Natural Science Foundation of China (Grant No. U22A20139, 12074373, 52072361, 12074374), Major Science and Technology Project of Anhui Province (Grant No. 2021e03020007), Key Research and Development Program of Jilin province (Grant No. 20210201024GX, 20220101208JC and 20230101123JC), Changchun science and technology planning project (Grant No. 21ZGY05), Youth Innovation Promotion Association CAS (No. 2020222), Opening Project of Key Laboratory of Transparent Opto-functional Inorganic Materials, Chinese Academy of Sciences .

Conflict of Interest

The authors declare no conflict of interest.

Author Contributions

L.Z., F.L., and J.Z. designed this project; X.L. synthesized the material and performed the measurement; D.W. performed the calculations and the related data analysis; D.W. contributed the SEM and TEM measurement; H.W., G.P., and H.W. contributed the photoluminescence spectrum analysis; L.Z., F.L., and J.Z. wrote the paper with contribution from all authors.

Open Research

Data Availability Statement

The data that support the findings of this study are available from the corresponding author upon reasonable request.

Supporting Information

Filename	Description
adfm202305275-sup-0001-SuppMat.pdf 2.2 MB	Supporting Information

Please note: The publisher is not responsible for the content or functionality of any supporting information supplied by the authors. Any queries (other than missing content) should be directed to the corresponding author for the article.

References

1 J. Cai, W. Zhang, L. Xu, C. Hao, W. Ma, M. Sun, X. Wu, X. Qin, F. M. Colombari, A. F. de Moura, J. Xu, M. C. Silva, E. B. Carneiro-Neto, W. R. Gomes, R. A. L. Vallée, E. C. Pereira, X. Liu, C. Xu, R. Klajn, N. A. Kotov, H. Kuang, *Nat. Nanotechnol.* 2022, **17**, 408.

CAS | PubMed | Web of Science® | Google Scholar

2 X. Ou, X. Qin, B. Huang, J. Zan, Q. Wu, Z. Hong, L. Xie, H. Bian, Z. Yi, X. Chen, Y. Wu, X. Song, J. Li, Q. Chen, H. Yang, X. Liu, *Nature* 2021, **590**, 410.

CAS | PubMed | Web of Science® | Google Scholar

3 C. Li, Q. He, Y. Wang, Z. Wang, Z. Wang, R. Annapooranan, M. I. Latz, S. Cai, *Nat. Commun.* 2022, **13**, 3914.

CAS | PubMed | Web of Science® | Google Scholar

4 Z. Xie, X. Zhang, Y. Xiao, H. Wang, M. Shen, S. Zhang, H. Sun, R. Huang, T. Yu, W. Huang, *Adv. Mater.* 2023, 2212273.

Google Scholar

5 Y. Bai, X. Guo, B. Tian, Y. Liang, D. Peng, Z. Wang, *Adv. Sci.* 2022, **9**, 2203249.

CAS | Google Scholar

6 S. Zhou, Y. Cheng, J. Xu, H. Lin, Y. Wang, *Adv. Funct. Mater.* 2022, **32**, 2208919.

CAS | Web of Science® | Google Scholar

7 Y. Zhuang, R.-J. Xie, *Adv. Mater.* 2021, **33**, 2005925.

CAS | PubMed | Web of Science® | Google Scholar

8 L. Liang, J. Chen, K. Shao, X. Qin, Z. Pan, X. Liu, *Nat. Mater.* 2023, **22**, 289.

CAS | PubMed | Web of Science® | Google Scholar

9 A. Qasem, P. Xiong, Z. Ma, M. Peng, Z. Yang, *Laser Photonics Rev.* 2021, **15**, 2100276.

CAS | Web of Science® | Google Scholar

10 B. Ren, B. Chen, X. Zhang, H. Wu, Y. Fu, D. Peng, *Mechanoluminescent optical fiber sensors for human-computer interaction*, Sci Bull, Beijing, 2023, **68**, pp. 542–545.

Google Scholar

11 H. J. Kim, S. Ji, J. Y. Han, H. B. Cho, Y.-G. Park, D. Choi, H. Cho, J.-U. Park, W. B. Im, *NPG Asia Mater* 2022, **14**, 459.

Google Scholar

12 Y. Fujio, C.-N. Xu, Y. Terasawa, Y. Sakata, J. Yamabe, N. Ueno, N. Terasaki, A. Yoshida, S. Watanabe, Y. Murakami, *Int. J. Hydrogen Energy* 2016, **41**, 1333.

CAS | Web of Science® | Google Scholar

13 B. Hou, L. Yi, C. Li, H. Zhao, R. Zhang, B. Zhou, X. Liu, *Nat. Electron.* 2022, **5**, 682.

Web of Science® | Google Scholar

14 Y. Ding, B. So, J. Cao, L. Wondraczek, *Adv. Sci.* 2022, **9**, e2201631.

Google Scholar

15 Y. Du, Y. Jiang, T. Sun, J. Zhao, B. Huang, D. Peng, F. Wang, *Adv. Mater.* 2019, **31**, 1970051.

Google Scholar

16 F. Han, T. Wang, G. Liu, H. Liu, X. Xie, Z. Wei, J. Li, C. Jiang, Y. He, F. Xu, *Adv. Mater.* 2022, **34**, 2109055.

CAS | Web of Science® | Google Scholar

17 J. Jia, X. Gao, G. Zou, *Adv. Funct. Mater.* 2022, **32**, 2207881.

CAS | Web of Science® | Google Scholar

18 T. Lyu, P. Dorenbos, P. Xiong, Z. Wei, *Adv. Funct. Mater.* 2022, **32**, 2206024.

CAS | Web of Science® | Google Scholar

19 L. Su, Q. Xiong, H. Wang, Y. Zi, *Adv. Sci.* 2022, **9**, 2203510.

CAS | Google Scholar

20 D. van der Heggen, J. J. Joos, A. Feng, V. Fritz, T. Delgado, N. Gartmann, B. Walfort, D. Rytz, H. Hagemann, D. Poelman, B. Viana, P. F. Smet, *Adv. Funct. Mater.* 2022, **32**, 2208809.

Google Scholar

21 C. Richard, B. Viana, *Light Sci Appl* 2022, **11**, 123.

CAS | PubMed | Web of Science® | Google Scholar

22 D. Peng, C. Wang, R. Ma, S. Mao, S. Qu, Z. Ren, S. Golovynskyi, C. Pan, *Kexue Tongbao (Foreign Lang. Ed.)* 2021, **66**, 206.

Google Scholar

23 C. Wang, R. Ma, D. Peng, X. Liu, J. Li, B. Jin, A. Shan, Y. Fu, L. Dong, W. Gao, Z. L. Wang, C. Pan, *InfoMat* 2021, **3**, 1272.

CAS | Web of Science® | Google Scholar

24 Y. Zheng, X. Li, R. Ma, Z. Huang, C. Wang, M. Zhu, Y. Du, X. Chen, C. Pan, B. Wang, Y. Wang, D. Peng, *Small* 2022, **18**, 2107437.

CAS | Web of Science® | Google Scholar

25 D. Peng, Y. Jiang, B. Huang, Y. Du, J. Zhao, X. Zhang, R. Ma, S. Golovynskyi, B. Chen, F. Wang, *Adv. Mater.* 2020, **32**, 1907747.

CAS | Web of Science® | Google Scholar

26 Z. Huang, B. Chen, B. Ren, D. Tu, Z. Wang, C. Wang, Y. Zheng, X. Li, D. Wang, Z. Ren, S. Qu, Z. Chen, C. Xu, Y. Fu, D. Peng, *Adv. Sci.* 2022, e2204925.

Google Scholar

27 Y. Zhuang, X. Li, F. Lin, C. Chen, Z. Wu, H. Luo, L. Jin, R.-J. Xie, *Adv. Mater.* 2022, 2202864.

Google Scholar

28 T. Zhou, H. Chen, J. Guo, Y. Zhao, X. Du, Q. Zhang, W. Chen, T. Bian, Z. Zhang, J. Shen, W. Liu, Y. Zhang, Z. Wu, J. Hao, *Small* 2023, **19**, 2207089.

CAS | Web of Science® | Google Scholar

29 T. Jiang, Y.-F. Zhu, J.-C. Zhang, J. Zhu, M. Zhang, J. Qiu, *Adv. Funct. Mater.* 2019, **29**, 1906068.

CAS | Web of Science® | Google Scholar

30 X. Wang, H. Zhang, R. Yu, L. Dong, D. Peng, A. Zhang, Y. Zhang, H. Liu, C. Pan, Z. L. Wang, *Adv. Mater.* 2015, **27**, 2324.

CAS | PubMed | Web of Science® | Google Scholar

31 X. Qian, Z. Cai, M. Su, F. Li, W. Fang, Y. Li, X. Zhou, Q. Li, X. Feng, W. Li, X. Hu, X. Wang, C. Pan, Y. Song, *Adv. Mater.* 2018, **30**, 1800291.

PubMed | Web of Science® | Google Scholar

32 J. Qin, H. Zhang, B. Lei, C. Hu, J. Li, Y. Liu, J. Meng, J. Wang, M. Zheng, Y. Xiao, *J. Am. Ceram. Soc.* 2013, **96**, 3149.

CAS | Web of Science® | Google Scholar

33 J. Botterman, K. van den Eeckhout, I. D. Baere, D. Poelman, P. F. Smet, *Acta Mater.* 2012, **60**, 5494.

CAS | Web of Science® | Google Scholar

34 P. F. Smet, J. Botterman, K. van den Eeckhout, K. Korthout, D. Poelman, *Opt. Mater.* 2014, **36**, 1913.

CAS | Web of Science® | Google Scholar

35 Y. Zhuang, Y. Lv, Wang Le, W. Chen, T.-L. Zhou, T. Takeda, N. Hirosaki, R.-J. Xie, *ACS Appl. Mater. Interfaces* 2018, **10**, 1854.

CAS | PubMed | Web of Science® | Google Scholar

36 Y. Zhuang, D. Tu, C. Chen, Wang Le, H. Zhang, H. Xue, C. Yuan, G. Chen, C. Pan, L. Dai, R.-J Xie, *Light Sci Appl* 2020, **9**, 182.

CAS | PubMed | Web of Science® | Google Scholar

37 R. R. Petit, S. E. Michels, A. Feng, P. F. Smet, *Light Sci Appl* 2019, **8**, 124.

CAS | PubMed | Web of Science® | Google Scholar

38 Z. Ma, J. Zhou, J. Zhang, S. Zeng, H. Zhou, A. T. Smith, W. Wang, L. Sun, Z. Wang, *Mater. Horiz.* 2019, **6**, 2003.

CAS | Web of Science® | Google Scholar

39 M. Kersemans, P. F. Smet, N. Lammens, J. Degrieck, W. Van Paepegem, *Appl. Phys. Lett.* 2015, **107**, 234102.

CAS | Web of Science® | Google Scholar

40 S. E. Michels, M. Kersemans, M. Versluis, G. Lajoinie, P. F. Smet, *Adv. Opt. Mater.* 2021, **9**, 2100085.

CAS | Web of Science® | Google Scholar

41 J. Qin, B. Lei, J. Li, Y. Liu, H. Zhang, M. Zheng, Y. Xiao, K. Chao, *ECS J. Solid State Sci. Technol.* 2013, **2**, R60.

CAS | Web of Science® | Google Scholar

42 M. Wang, X. Zhang, Z. Hao, X. Ren, Y. Luo, H. Zhao, X. Wang, J. Zhang, *J. Electrochem. Soc.* 2010, **157**, H178.

CAS | Web of Science® | Google Scholar

43 T. Aitasalo, J. Hölsä, H. Jungner, J.-C. Krupa, M. Lastusaari, J. Legendziewicz, J. Niittykoski, *Radiat. Measur.* 2004, **38**, 727.

CAS | Web of Science® | Google Scholar

44 V. Chernov, R. Meléndrez, M. Pedroza-Montero, W. M. Yen, M. Barboza-Flores, *Radiat. Measur.* 2008, **43**, 241.

CAS | Web of Science® | Google Scholar

45 K. van den Eeckhout, A. J. J. Bos, D. Poelman, P. F. Smet, *PhRvB* 2013, **87**, 515.

Google Scholar

46 G. F. J. Garlick, A. F. Gibson, *Photochem Photobiol Sci* 1948, **60**, 574.

CAS | Google Scholar

47 G. Kitis, J. M. Gomez-Ros, J. W. NTuyn, *J. Phys. D: Appl. Phys.* 1998.

Google Scholar

Citing Literature

Download PDF